JOINT EUROPEAN TORUS

JET–P(91)20

The JET Team
presented by J. Jacquinot

Heating, Current Drive and Confinement Regimes with the JET ICRH and LHCD Systems

Heating, Current Drive and Confinement Regimes with the JET ICRH and LHCD Systems

The JET Team*
presented by J. Jacquinot

JET-Joint Undertaking, Culham Science Centre, OX14 3DB, Abingdon, UK

** See Appendix 1*

Preprint of Paper to be submitted for publication in
Plasma Physics and Controlled Fusion

HEATING, CURRENT DRIVE AND CONFINEMENT REGIMES WITH THE JET ICRH AND LHCD SYSTEMS

The JET Team[1] presented by J Jacquinot

JET Joint Undertaking, Abingdon, Oxon, OX14 3EA, UK

ABSTRACT

During its 1990 operation, 2 large RF systems were available on JET. The Ion Cyclotron Resonance Heating (ICRH) system was equipped with new Beryllium screens and with feedback matching systems. Specific impurities generated by ICRH were reduced to negligible levels even in the most stringent H-mode conditions. A record power of 22 MW was coupled to the plasma. High quality H-modes ($\tau_E \geq 2.5\ \tau_{EG}$) were achieved using dipole phasing. A new high confinement mode was discovered. It combines the properties of the H-mode regime to the low central diffusivities obtained by pellet injection. A value of $n_d\ \tau_E\ T_i = 7.8 \times 10^{20}\ m^{-3}$ s keV was obtained in this mode with $T_e \sim T_i \sim 11$ keV. In the L-mode regime, a record (140 kW) D-^{3}He fusion power was generated with 10 - 14 MW of ICRH at the ^{3}He cyclotron frequency.

Experiments were performed with the prototype launcher of the Lower Hybrid Current Drive (LHCD) systems with coupled power up to 1.6 MW with current drive efficiencies up to $0.4 \times 10^{20}\ m^{-2}$ A/W. Fast electrons are driven by LHCD to tail temperatures of 100 keV with a hollow radial profile. Paradoxically, LHCD induces central heating particularly in combination with ICRH. Finally we present the first observations of the synergistic acceleration of fast electrons by Transit Time Magnetic Pumping (TTMP) (from ICRH) and Electron Landau Damping (ELD) (from LHCD). The synergism generates TTMP current drive even without phasing the ICRH antennae.

1. NEW HARDWARE, UNDERLYING PHYSICS AND OUTLINE

The subject of this article is a review of the results obtained with the new Radio Frequency and microwave high power equipments which were made available when JET started its 1990 experimental campaign.

1.1 New Hardware. A prototype Lower Hybrid Current Drive Launcher (Gormezano et al, 1991) was operated for the first time in JET. The system was fed by 8 klystrons at 3.7 GHz and could couple 1.6 MW to the plasma with 128 waveguides in the form of a travelling wave with an adjustable wave index $1.6 < n_{\parallel} < 2.3$. The system is still in a conditioning phase and the power was limited by arcing or cross-talking in the waveguides. The launcher could be moved during the shot using hydraulic actuators so that the reflected power could be minimized. Significant non-inductive current drive could be generated (> 1 MA). The initial experiments give new information on the creation of fast electrons and on the current drive efficiency in reactor size plasmas at high electron temperature.

The Ion Cyclotron Resonance Heating (ICRH) system was upgraded to a total generator power of 32 MW and the screens of the 8 antennae previously made of nickel bars were replaced by screens equipped with Beryllium bars. The screen design was optimized in order to eliminate impurity release from self-sputtering of the screen by ions accelerated in the electric field produced by RF field rectification in the Bohm sheath (Bures et al, 1990, D'Ippolito et al, 1991, Chodura et al, 1990). Further description of the screens is given in the sections "H-modes" and "Edge Effects".

[1] For list of authors, see JET Team presented by M Keilhacker, these proceedings.

Table 1: The JET RF System

	ICRH	LHCD	
		Prototype	Full System
Frequency	23 to 57 MHz	3.7 GHz	3.7 GHz
Power (MW)	16 amplifiers	8 klystrons	24 klystrons
• Generator	32	5	15 MW in total
• Coupled (1990)	22.3	1.6	to be installed in 1992
Antennae	8 modules Beryllium screens Dipole or monopole phasing Wall mounted	128	384 waveguides multijunction type $1.6 < n_{\|\|} < 2.3$ located in one horizontal port
Matching	3 feedback loops: frequency, stub, plasma position	launcher moveable during the pulse	

Three feedback control systems could be operated simultaneously. They act on the impedance transformation (frequency and stub length) as well as on the radial plasma position so that the generators no longer experience large changes of load impedance during a pulse. The system was particularly useful during H-mode studies. The upgrades of the antenna screen and the feedback systems allowed a new higher power to be coupled to plasmas (22.3 MW in L-mode, 14 MW in H-mode). The specific impurities produced by ICRH were negligible in all conditions.

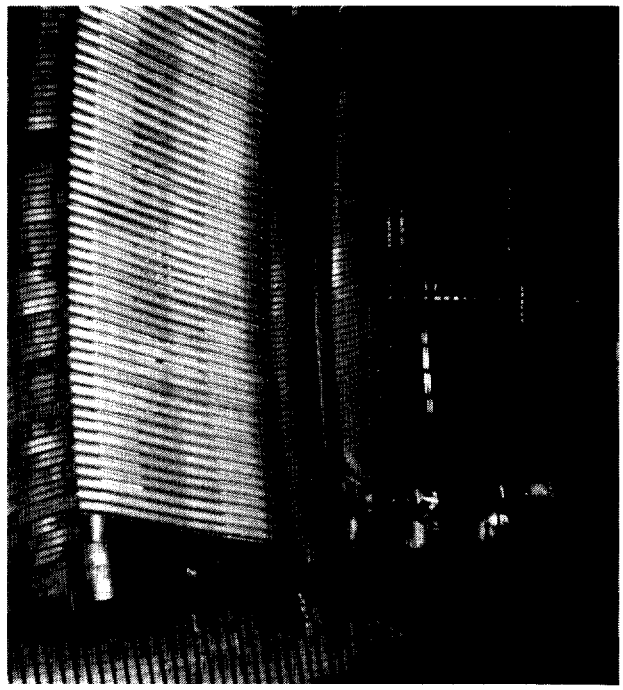

Fig. 1: One of the 8 ICRH antenna equipped with tilted beryllium screen bars can be seen on the left. The LHCD launcher is on the right (2 modules of 64 waveguides each). The Beryllium tiles of the belt limiters are visible on the top and bottom parts of the picture.

Table 1 summarizes the main aspects of the LHCD and ICRH systems. Other aspects of these systems can be found elsewhere (Pain et al, 1989, Jacquinot et al, 1988).

Figure 1 shows the LHCD launcher and one of the 8 ICRH antennae side by side. The LHCD launcher occupies a main horizontal port; the ICRH antenna are mounted on the vessel wall and each antenna uses 2 small cylindrical penetrations (ϕ = 14 cm) for the co-axial feeding lines.

1.2. Underlying Physics.

The 2 RF systems have been conceived on the following different underlying physics mechanisms.

The Lower Hybrid waves are slow waves. The wave propagates at a small angle with the magnetic field line and the wave length in the plasma is quite small ($\sim 2 \times 10^{-3}$ m). The wave electric field is nearly parallel to the magnetic field and the wave is damped by Electron Landau (EL) damping giving parallel energy to plasma electrons moving with the speed corresponding to the wave phase velocity. The wave cannot penetrate (due to accessibility and damping conditions) further than a critical density $n_{e\,crit}$. In JET, $n_{e\,crit}$ is about $2 \times 10^{19} m^{-3}$.

The ICRH system launches fast waves. The wave propagates nearly along the density gradient and focuses near the magnetic axis; the wave length is much larger (0.1 to 0.2 m). The wave electric field is nearly perpendicular to the magnetic field and the principal wave damping mechanism is by cyclotron acceleration giving perpendicular energy to a chosen minority ion species (^{3}He or H in this work). In most cases the cyclotron resonance is adjusted to be on the magnetic axis and the power deposition in centrally peaked. There is no limit to the density that the wave can penetrate. Recently another weaker damping mechanism, the Transit Time Magnetic Pumping (TTMP) has been demonstrated in JET (Start et al, 1990). It can only be significant in large plasmas with a high electron temperature, or as in this work, when fast electrons are present. TTMP damping communicates parallel energy to the electrons similar to EL damping of Lower Hybrid Waves; however, in this case, the force acting on the electrons is $\mu \nabla_{\parallel} \tilde{B}$, μ = electron magnetic moment, $\tilde{B}$ = RF magnetic field (and not $e\tilde{E}_{\parallel}$, $\tilde{E}$ = RF electric field) as with lower hybrid waves. In both cases electron current drive is predicted. Figure 2 sketches the basic physics interactions. Note that both systems create fast particles. Fast electrons in the case of EL or TTMP damping and fast minority ions in the case of ICRH.

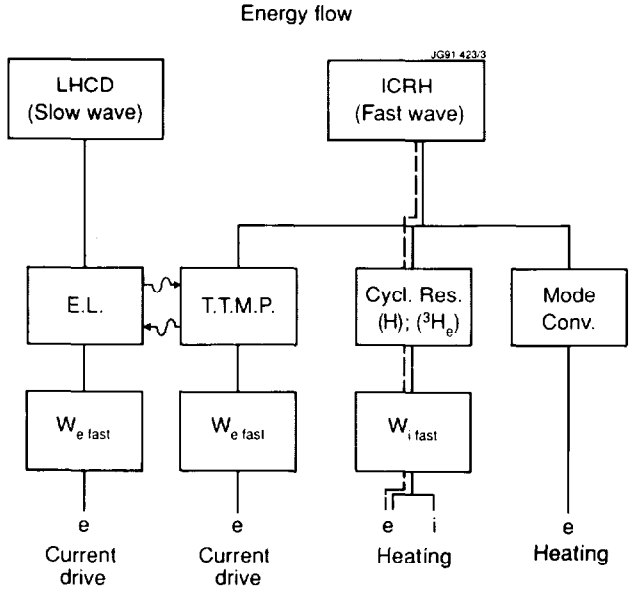

Fig 2: Energy flow diagram for the slow wave used by LHCD and the fast wave used by ICRH. The damping mechanisms are: EL = Electron Landau damping; TTMP Transit Time Magnetic Pumping; the cyclotron resonance of a minority H or ^{3}He and mode conversion. The usual route for ICRH is represented by the dotted line. Synergism can link EL from LHCD and TTMP from ICRH

1.3. Outline.

This paper is organized in the following way:

The results on current drive and electron heating using Lower Hybrid waves are first presented. The emphasis is placed on the localisation of the Lower Hybrid waves taking advantage of the large dimensions of the JET plasma and of a camera detecting bremsstrahlung radiation emitted by the fast electrons. The current drive efficiency is measured in plasmas preheated by ICRH at various power levels. Lack of space prevents us discussing other aspects of LHCD such as antenna coupling and the fast electron dynamics. The interested reader is referred to other contributions on these subjects presented at this conference (Gormezano et al, 1991; Moreau et al, 1991; Froissard et al, 1991).

The following section is devoted to the synergistic interaction between LHCD and ICRH which appears on nearly all observable quantities. It is the first observation of this kind. The interaction was expected as the TTMP from the fast wave can effectively be coupled to the fast electrons created by the Lower Hybrid waves. The mechanism opens new routes to enhance the current drive and to higher central electron heating capability of JET.

In the succeeding section, we focus our attention on the confinement regimes achieved with ICRH. The L-mode regime has been explored at higher power and has given rise to record performance in the D-^{3}He advanced fuel scenario. Long H-modes have been produced both with monopole and dipole phasing; the highest performance being obtained when the H-mode regime is combined with deep pellet fuelling.

We finally review the ICRH edge effect observed with beryllium screens. Although beryllium has removed all deleterious impurity effects, we argue that the basic sheath RF rectification mechanism is still at work when the monopole phasing is used and that a convective cell is generated.

2. LOWER HYBRID WAVES IN LARGE JET PLASMAS, LOCALISATION OF FAST ELECTRONS AND THE CURRENT DRIVE EFFICIENCY

The penetration of lower hybrid waves in tokamak plasmas and the mechanism for fast electron production is a complex subject. The antenna launches a beam with a well-defined parallel spectrum. In JET, the $n_{\parallel}$ spectrum is formed by the phasing of 16 waveguides side by side in the toroidal direction; consequently the $n_{\parallel}$ is quite peaked; typically $n_{\parallel} = 1.8 \pm 0.2$. Landau damping, the dominant damping process for LH waves, implies $\omega = k_{\parallel}V_{\parallel}$ or $V_{\parallel} = c/n_{\parallel}$, meaning that the wave is resonant with 100 keV electrons. There is therefore a considerable "gap" between thermal electrons and resonant electrons, and a simple linear theory would predict no absorption at all. Recent theories based on the broadening of the launched spectrum due to toroidal effects on waves undergoing multiple reflections (Bonoli and Englade, 1986; Moreau et al, 1989) have had some success in modelling the bridge of the gap which is observed experimentally. For instance, Fig. 3 gives the results of calculations (Brusati et al, 1989) of the Lower Hybrid driven current showing that the wave damping is excluded from the plasma centre when $n_{eo} > 2.5 \times 10^{19}$ m^{-3}. When n_{eo} reaches 5×10^{19} m^{-3} the wave interacts only with the periphery.

This predicted behaviour is qualitatively observed with a camera detecting the bremsstrahlung radiation emitted by fast electrons (Froissard et al, 1991). The local emissivity is quite hollow and the hollowness increases with density (Fig. 4). The Fast Electron Bremstrahlung (FEB) camera can also resolve the energy of the received photons. It detects a "temperature" of photons of about 100 keV. A similar high energy tail is observed from the hard X-ray energy spectrum obtained by X-ray pulse height analysis using a Germanium detector.

The current drive efficiency is corrected downwards to take account of the effect of the remaining electric field. The efficiency is defined as $\gamma = < n_e > RI_{CD}/P_{CD}$ where $P_{CD} = P_{LH} + I_{CD}V_{loop}$ and n_e is the line average density.

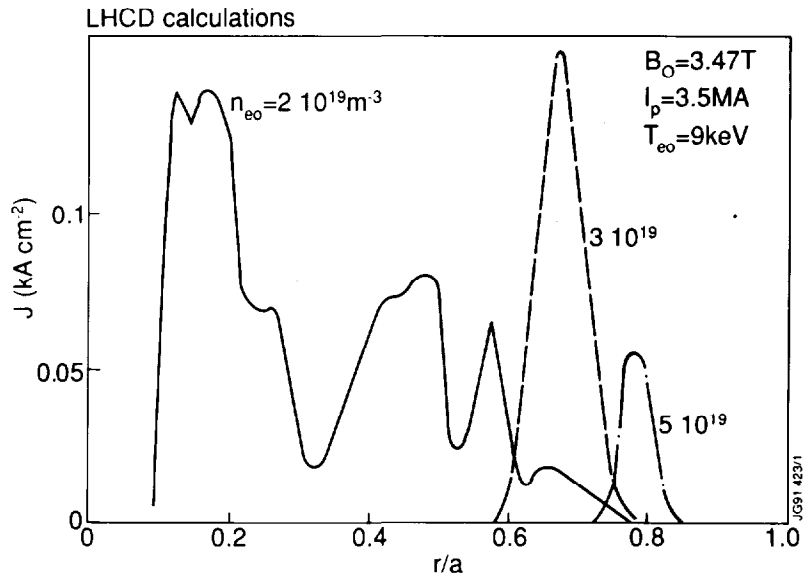

Fig 3: Calculated current drive profile (Bonoli code) expected from LHCD. The central density for each case is indicated.

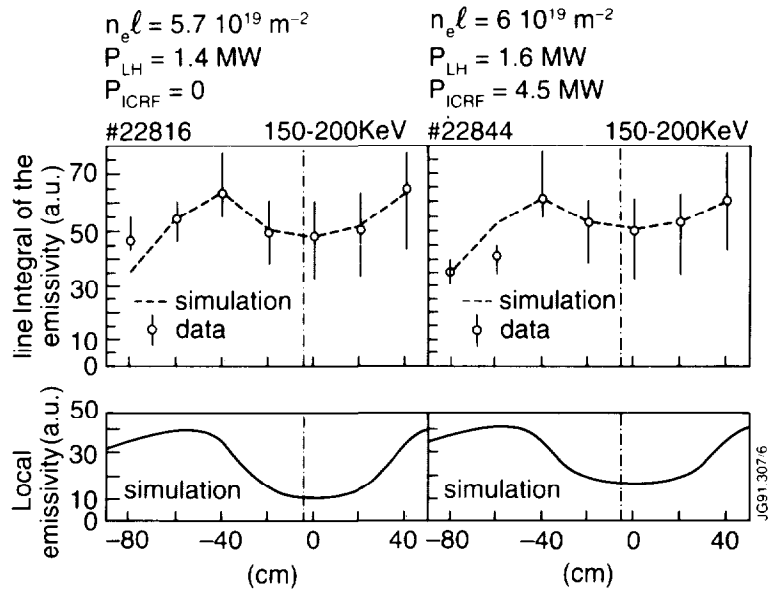

Fig 4: Line integral emissivity for photon energy in the 150-200 keV range versus the radial position. The distribution of the fast electrons is hollow. The hollowness increases with energy and electron density.

The efficiency γ increases sharply when the plasma is preheated by ICRH (Fig. 5). Non-inductive currents up to 1.2 MA are driven when $< T_e > = 1.9$ keV ($P_{ICRH} \sim 4$ MW) and g reaches $\sim 0.45 \times 10^{20}$ m^{-2} A/W. A linear increase of γ with T_e has already been reported by JT-60 (Ushigusa et al, 1990) and is derived from models where the power spent to fill the spectral gap is reduced when the electron temperature increases. In our experiments, the increase with T_e is even faster than linear and there is no sign of saturation when the maximum theoretical efficiency is reached. The achieved g values are the highest ever achieved in current drive experiments. In the next paragraph, we point out that the real efficiency may have to be reduced somewhat in order to take into account some spontaneous gift from TTMP current drive from ICRH.

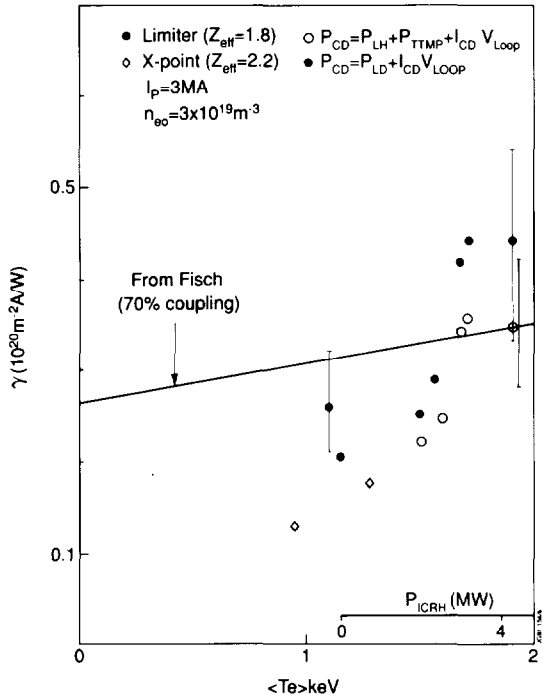

Fig 5: Normalised current drive efficiency $\gamma = I_{CD} < n_e > R/P_{CD}$. Solid points are with $P_{CD} = P_{LH} + I_{CD} V_{loop}$. Open circles with $P_{CD} = P_{LH} + P_{TTMP} + I_{CD} V_{loop}$.

3. THE SYNERGY BETWEEN LHCD AND TTMP (FROM ICRH)

The $n_{||}$ spectrum of the fast waves launched by the ICRH system in the monopole phasing mode broadly extends from $n_{||}$ = -4 to +4. Therefore the wave phase velocity overlaps the entire energy spectrum of the fast electrons created by LHCD and some of the wave energy which should have been damped by cyclotron resonance on minority ions may now be damped by TTMP on the unidirectional fast electrons, reinforcing the non-inductive current without having to phase the ICRH antennae.

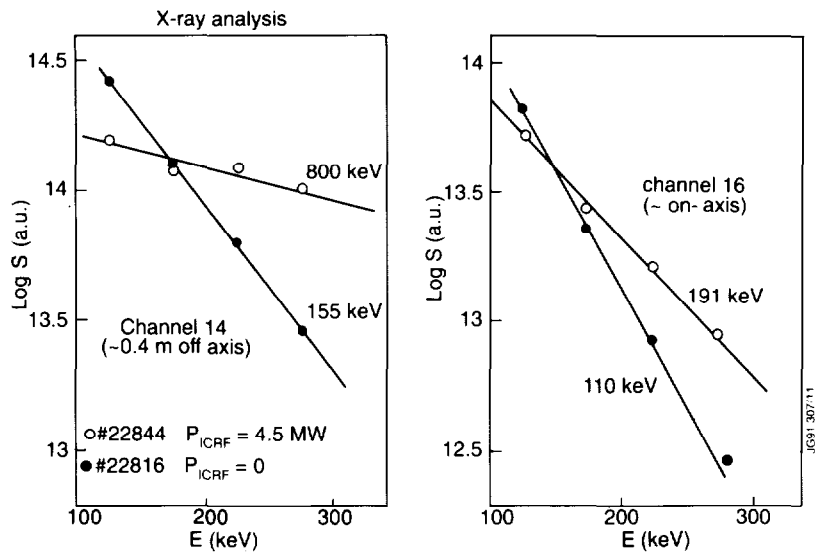

Fig 6: Photon distribution versus photon energy measured perpendicularly to the toroidal field. The lines of sight cross the equatorial plane either on-axis or 0.4 m off-axis. The LHCD power is 1.2 MW and the ICRH power is either 0 (solid points) or 4.5 MW (open circles). The synergistic effect is most pronounced in the densest region of fast electrons.

Synergism on the fast electron production is quite apparent on all 8 viewing lines of the FEB camera. The "photon temperature" is raised from 100 keV to 200 keV on most channels (Fig. 6). The highest rise of the "photon temperature is observed where the density of the fast electrons is the highest. This increase appears slowly and takes about 0.5 s to develop at 300 keV. The radial profile of the fast electrons remains hollow but tends to fill in the centre (Fig. 4).

Synegistic effects can also be observed on the central electron temperature which is, for a given total power, higher and more peaked with the combination of LHCD and ICRH (Fig. 7) and on the central heating rate (Fig. 8) measured from modulation of the Lower Hybrid power at fixed ICRH power levels.

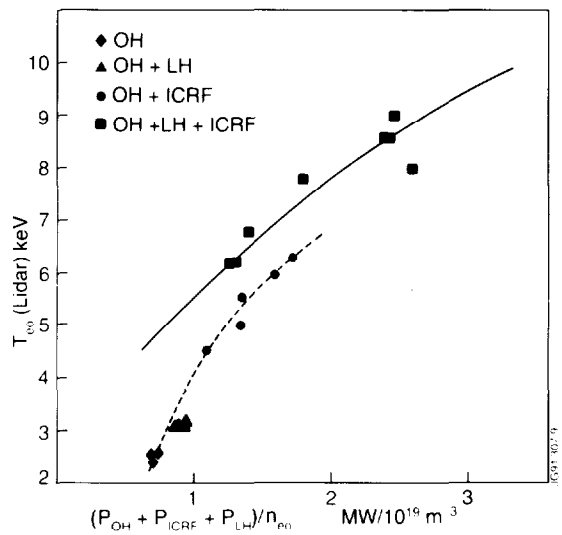

Fig.7: Central electron temperature from Thomson scattering versus the total input power showing the synergistic effect on the cental electron temperature

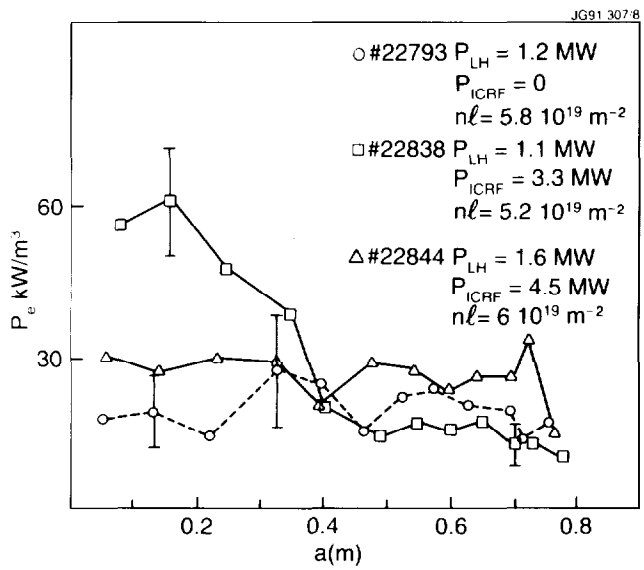

Fig 8: Direct electron heating rate deduced from measurements of dT_e/dt during modulation of the LH power. Integrating these curves, we find that about 10 % of the ICRH power has been diverted from the usual minority resonance absorption to direct electron heating from TTMP.

Neglecting the effects of transport in the modulation experiments of Fig. 8, we find that the synergistic TTMP current drive power is of the order of 400 kW, eg about 10 % of the ICRH power. Logically, our estimate of γ given in the last section should be reduced from 0.45×10^{20} to 0.35×10^{20} when P_{CD} now includes the TTMP power $P_{CD} = P_{LH} + P_{TTMP} + I_{CD}V_{loop}$. The amount of current driven by TTMP is estimated to be about 250 kA.

The modelling with a 3D Fokker Planck code of this synergistic process is in progress (O'Brien and Cox, 1991). Initial results show that the level of interaction found is plausible. We finally suggest that the interaction (and therefore the TTMP current drive) could be enhanced by removing the cyclotron resonance from the plasma centre using for instance the following parameters: 32 MHz, 3.1 T and no ^{3}He minority in the plasma.

4. CENTRAL ELECTRON HEATING WITH ICRH

Several experiments have been directed at raising the electron temperature to a high value by maximising the total input power per particle (P/n). The maximum temperature T_{eo} reached 13 keV (Fig. 9) in long sawtooth-free discharges (7 s at I_p = 3.5 MA) with significant ^{3}He minority concentration (0.05 - 0.1). In other experiments, T_{eo} saturates when P/n exceeds $4\ 10^{-19}$ MW/m^{-3} (Fig. 10). Cordey et al, 1991 have expressed the electron heating rate due to the collisional slowing down of the minority ions in terms of $P_{eff} \alpha W_{fast}/\tau_s(0)$ where W_{fast} is the energy stored in the fast ions and $\tau_s(0)$ is the central fast ion slowing down time. It was noticed that the central electron temperature correlates well with P_{eff}. The conclusion of the study is that the central ion and electron confinement properties in L-mode are similar. However, the central electron heating using minority ion heating with ICRH may be limited by 2 broadening effects.

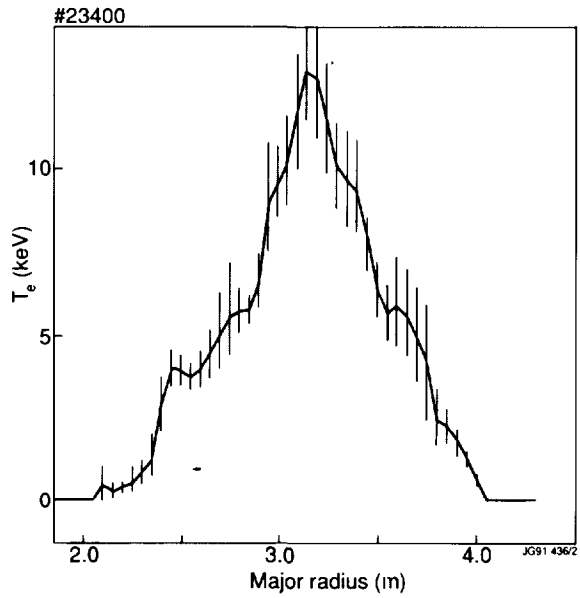

Fig 9: Electron temperature profile during ICRH heating (P_{ICRH} = 11.4 MW) in an experiment with the highest central electron temperatures.

a) **Broadening from finite Larmor radius (FLR)** of the trapped minority ions with a guiding centre describing fat bananas (Cottrell and Start, 1991; Eriksson et al, 1991; Kovanen and Core, 1990). This effect will be significant when the width of the banana becomes comparable to the width of the ICRH power deposition (W_{RF}):
eg: $$(r/a)^{1/2}\rho_o \sim W_{RF} \quad (1)$$

where ρ_o is the Larmor radius in the poloidal field. Since the energy of the fast ion tail depends on the minority concentration, this effect can be made small at high minority concentration. Using the expression for the Stix

tail (Stix, 1975), we find that the minimum concentration should be:

$$\eta = \frac{n_{min}}{n_e} > \frac{P}{Zen_e^2} \cdot \frac{3.95 \times 10^{13}}{T_{crit}} \cdot \frac{A}{Z^2} T_e^{3/2}(eV) \qquad (2)$$

with $T_{crit} = \frac{eW_{RF}}{2RAm_p} \cdot \left(W_{RF} Z \frac{B}{q} \right)^2$

For instance, take $W_{RF} = 0.35$m, $T_e = 10$ keV, $n_e = 2 \times 10^{19}$ m^{-3}, then Eq.(2) is satisfied for $\eta > 0.04$.

b) **Anomalous Broadening**. There are other physical effects that can give rise to the broadening of the fast ion radial profile: sawteeth, fishbones, Alfvén or drift wave turbulence driven by the pressure anisotropy or by large ion pressure gradients.

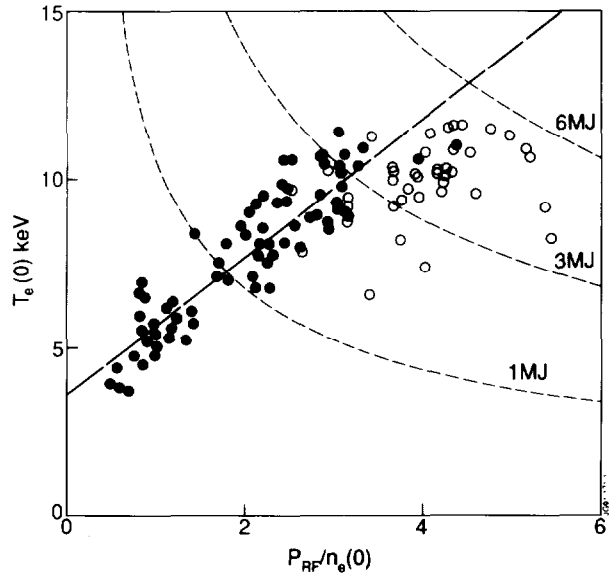

Fig 10: Central electron temperature versus $P_{RF}/n_e(o)$. The measured power deposited within the half-width of the temperature profile is within 30 % of the applied power for the solid points and outside this range for the open points. The contour refer to the fast ion energy content required to provide the required T_{eo} at normalized central heating power $P/n_e(0)$.

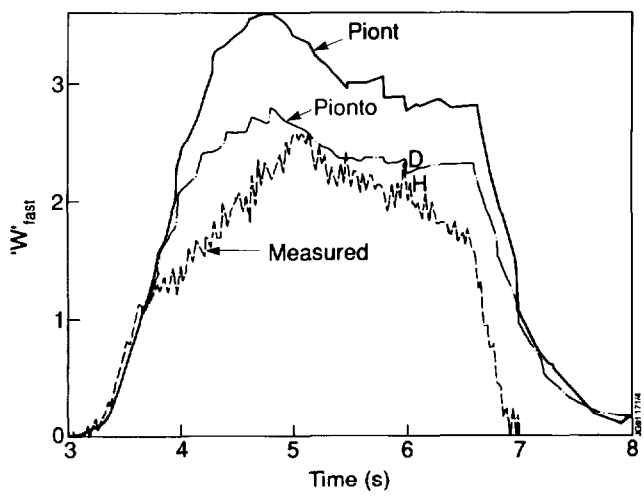

Fig 11: Fast ion energy versus time and comparison to simulation codes. P_{IONT} describes the fast ions with a zero banana width Fokker Planck solver. P_{IONTo} includes an approximate orbit model

In JET, there is clear evidence that both sawteeth and fishbones can expel fast ions from the central region. In discharges with the largest T_{eo}, these effects are not always observed, but the broadening due to FLR effects can be significant. Figure 11 shows that the observed evolution of W_{fast} differs from code calculations without FLR effects. Similar estimates of FLR broadening has been obtained by different approaches (see figure caption of Fig. 11).

It is important to note that to obtain $T_e(0) = 20$ keV in JET with the same L-mode confinement requires a fast ion energy content in excess of 12 MJ equivalent to a central toroidal $\beta_{fast} \sim 24$ %. It is likely that instabilities will prevent such a state from being reached.

Excessive pressure build-up in fast ions constitutes a fundamental limitation for central electron heating in low magnetic field tokamaks at high power. It is possible to remove this limitation by using direct electron heating with TTMP from ICRH or EL from LHCD. However, even with these methods, a fast electron minority ion damping in discharges with the highest T_{eo}. For instance, for the conditions of Fig. 9 with $T_{eo} = 13$ keV, TTMP damping amounts to $\simeq$ 15 % of the total wave damping.

5. D-^{3}He FUSION EXPERIMENTS

Progress has been made in the optimisation of the D-^{3}He fusion yield during a new series of experiments using the ICRF heating system with frequency adjusted to the ^{3}He ion cyclotron resonance near the magnetic axis (Sadler et al, 1991; Jacquinot and Sadler, 1991). Best results were obtained with 3.5 MA discharges in the double null configuration with the wall power loading being shared between X-point dump plates, the belt limiter and antenna protection tiles. The discharge is maintained in L-mode in order to control the central density to about 2.5 10^{19} m^{-3} and reach large values of T_{eo} (the temperature profile of Fig. 9 was obtained during this series, see also Fig. 12). The concentration of the minority ^{3}He ions was controlled either by gas puffing and/or using central ^{3}He deposition by the NBI system. The concentration $n_{^3He}/n_e$ was varied between 0.03 and 0.15. The best results were obtained without the ^{3}He NBI injection presumably because the optimum concentration was rapidly exceeded with NBI.

The generated ^{3}He-D fusion power increased to 140 kW (corresponding to a reaction rate of 4.6×10^{16} reactions/s) using 14 MW of ICRH power. The fusion multiplication factor $Q_{RF} = P_{FUS}/P_{RF}$ reached 1.25 %. The highest values of Q_{RF} were obtained with P_{RF} in the range of 10 to 12 MW.

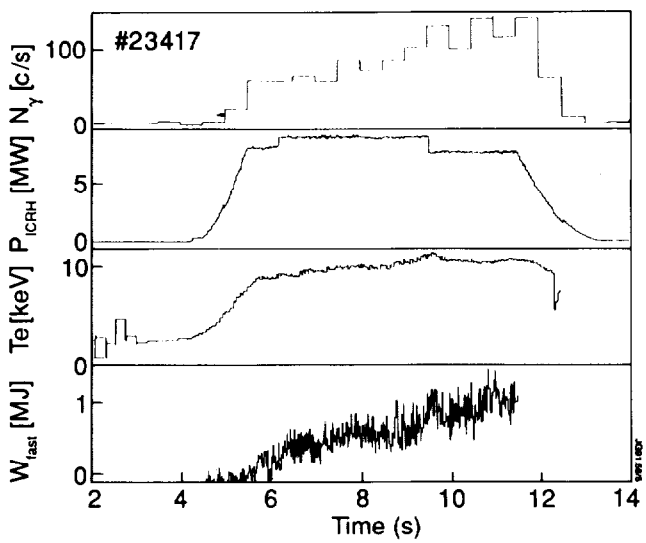

Fig 12: Evolution of the 14 MeV γ count, ICRH power, central electron temperature and energy stored in the fast particles during a D-^{3}He fusion experiment

A clear correlation between the generated fusion power and energy stored in the fast ^{3}He ions is observed (Figs. 12 and 13): The maximum yield $(P_{fus})_{MAX}$ scales linearly with W_{fast}.

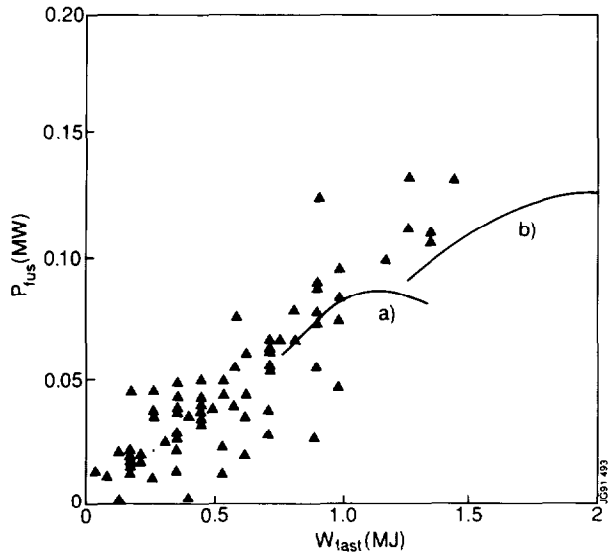

Fig 13: D-^{3}He fusion yield versus the perpendicular energy of the fast ^{3}He ions determined from magnetic measurements ($W_{fast} = 4(W_{dia} - W_{MHD})/3$). Comparison to calculations: curve (a) T_{eo} = 8 keV, P (power to ^{3}He) = 7.5 MW; curve (b) T_e = 10 keV, P = 10 MW. The curves are obtained by varying the ^{3}He concentration and the maximum of curve (a) corresponds to $n_{^3He}/n_e$ = 0.05.

A theoretical model has been developed (Jacquinot and Sadler, 1991). Based on the Stix anisotropic distribution function, the model takes into account the various profiles of the RF power deposition and of the plasma parameters (T_e, n_e, Z_{eff}). It is possible to express the results of the calculation in the following way:

$$(P_{fus})_{MAX} = \alpha F(n_d, n_e) W_{fast} \qquad (3)$$

where $(P_{fus})_{MAX}$ is the fusion yield obtained for the optimum ^{3}He concentration and α is a coefficient which varies only weakly with the other plasma parameters (including profiles) $\alpha \simeq 0.1$ to 0.2 s^{-1}. The optimum concentration invariably corresponds to a "tail temperature" of the minority which is close to 1 MeV in order to match the optimum fusion cross-section. It is clear from Fig. 13 that the maximum yield observed in JET is close to the maximum possible yield for the observed values of W_{fast} and of n_d/n_e. It is therefore possible to conclude that the optimum ^{3}He concentration corresponding to a 1 MeV tail was reached during these experiments.

6. CONFINEMENT REGIMES WITH ICRH

The elimination of specific ICRH impurities and the system upgrades in power and control have opened the exploration of new confinement regimes and the extension of the power level in the regimes previously obtained.

6.1.L-mode Regime. We have already discussed some results obtained in this regime under 'Central Electron Heating' and 'D-^{3}He Fusion Experiments', we now concentrate on results concerning global energy confinement.

The power scan using ICRH only has been extended to a total loss power of 23 MW. The results summarized on Fig. 14 shows the results of a scan where the plasma current was 3 MA, $B_\phi = 2.8$ T and the volume averaged density was in the range of 2 to 5 10^{19} m^{-3}. The plasma was resting on the beryllium belt limiters. Z_{eff} was in the range

1.5 to 2.5 and P_{rad}/P_{tot} ~ 0.1 to 0.3. Hydrogen minority and dipole phasing were used. Energy stored in the fast ions in these discharges is small (≤ 10 %) due to operation at higher density especially at higher power level. It can be seen that the performance is somewhat better than the value given by the Goldston (Goldston, 1984) regression fit. $\tau_E = 1.3\ \tau_{EG}$. We should stress that in these experiments, the power deposition was always close to the axis (resonance in the centre) and the sawtooth duration was larger or comparable to the energy confinement time.

6.2. H-mode Regime. The first H-modes with ICRH alone on JET were obtained (Jacquinot et al, 1990; Tubbing et al, 1990; Start et al, 1990; Bhatnagar et al, 1991) using dipole phasing and beryllium evaporation on nickel screens ("opaque design"). Generally the performance was similar to H-mode generated by NBI although nickel radiation was still a significant fraction of the total radiated power.

No H-mode had been generated using monopole phasing and Nickel screens. All the experiments reported here use the new Beryllium screens. The design is based on simple solid Beryllium bars cooled at the 2 ends by conduction. The screen is open with a transparency of 25 %. The screen bars are tilted by 15° and are shaped toroidally in a shallow "V". The choice of beryllium, the 15° tilt and the "V" shape are based on the physics of specific ICRH impurity generation (D'Ippolito et al, 1990) which gives guidelines to minimize the sheath potential due to RF field rectification. This geometry is chosen to cancel all RF sheath effects in dipole phasing. In monopole phasing, the cancellation can never be perfect due to some remaining misalignment with the magnetic field lines.

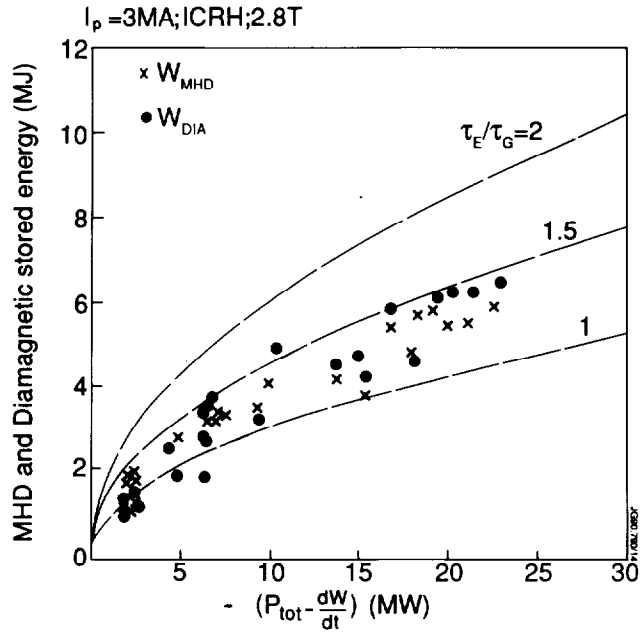

Fig 14: MHD and diamagnetic stored energy versus loss power during ICRF heating of L-mode plasmas up to 23 MW.

The 3 feedback loops (frequency, stubs and plasma position) which constitute the plasma-antenna matching system are particularly useful to handle the large changes in the scrape-off plasma during H-mode transitions or during ELMs. The frequency and plasma position feedback system have a time response of 1 ms and 30 ms respectively. These reaction times are sufficiently short to smooth out variations of the antenna loading due not only to H-mode transitions but also to sawteeth. Figure 15 shows the adjustments of plasma radial position and RF frequency necessary to maintain the antenna loading constant. It can be seen in Fig. 15 that the time constant imposed by H-mode transitions is typically 20 ms. Since the antenna loading is a complex number, it is essential to react on 2 quasi-independent variables. The plasma position feedback loop maintains constant the real part of the antenna impedance (the error signal is constructed from measurements of the antenna loading resistance). During the H-mode transition, the plasma is moved towards the antenna by 1 to 2 cm. It is remarkable, that H-modes of the highest quality could be maintained with a distance between the separatrix and the antenna side protection as low as 1 cm. However, to obtain the H-mode, one needs to start in L-mode with a separation of about 2.5 cm (Fig. 15).

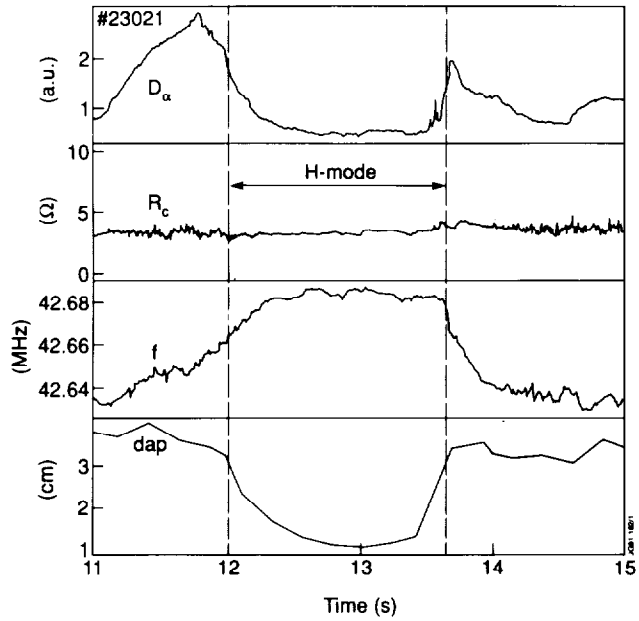

Fig 15: D_α emission, antenna loading resistance, RF frequency and distance (d_{ap}) between separatrix and antenna side protections during an ICRH H-mode. Both the frequency and d_{ap} are under feedback control to maintain the real and imaginary parts of the loading resistance constant.

6.3. H-mode with Dipole or Monopole Phasing. H-modes produced by ICRH alone with monopole or dipole phasing present the usual typical characteristics (Bhatnagar et al, 1991): the D_α emission drops by a factor 10, the density increases, the total radiation first decreases then increases steadily. More importantly, the stored energy rises above its L-mode value. The D-D reaction rate

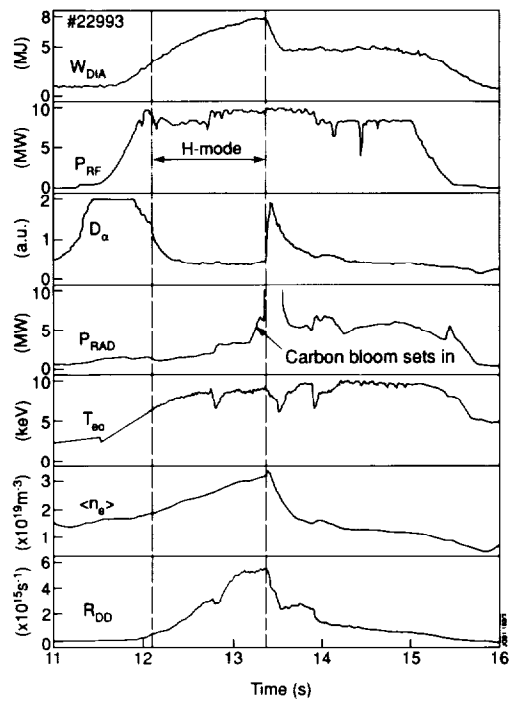

Fig 16: Time traces of a high performance ICRH H-mode with dipole phasing. $\tau_E \simeq 2.8\ \tau_{EG}$ (including fast particles).

(R_{DD}) rises in the best dipole H-modes to about 5 to 10 times the L-mode value at the same current and for the same power. Figure 16 illustrates the characteristic signals in a dipole H-mode where the diamagnetic stored energy rises to a value corresponding to 2.8 τ_{EG} where τ_{EG} is the value derived from the Goldston (Aachen) scaling. The H-mode transition occurs in one or several steps. The return to the L-mode is normally (as in Fig. 16) caused by a carbon "bloom" caused by excessive loading of the carbon target plates located in the X-point region.

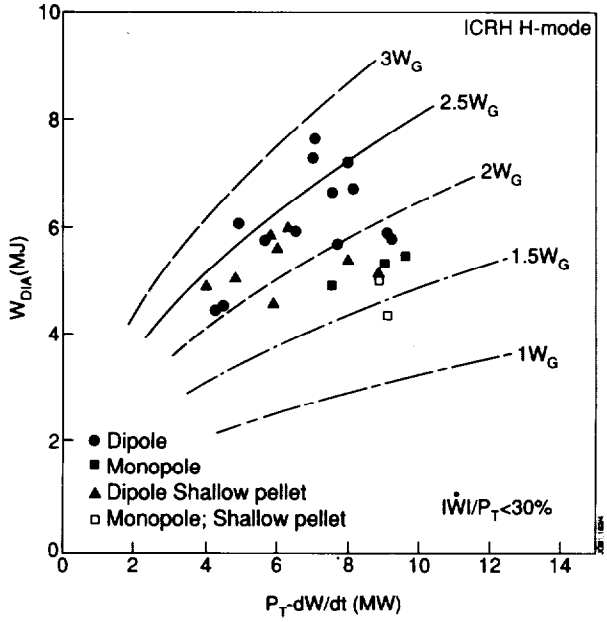

Fig 17: Diamagnetic stored energy versus loss power with dipole and monopole phasing. The energy stored in the fast particles amount to about 1 MJ for the points with the highest W_{dia}. Comparison to Goldston scaling (W_G).

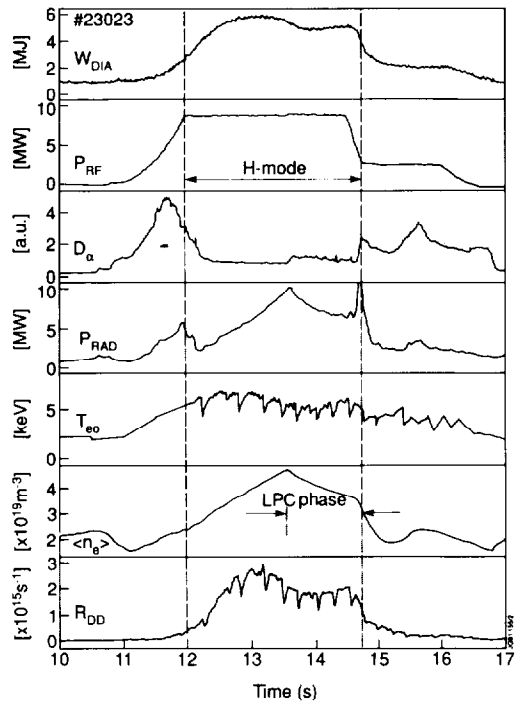

Fig 18: Time traces of an H-mode with dipole phasing and gas injection in the X-point region; at 13.5 s a transition to a low particle confinement phase (LPC) occurs with reduction of Z_{eff} and P_{rad} at the expense of some loss of stored energy.

H-modes produced with monopole phasing have similar evolution of the D_α emission but have clearly an inferior performance: the diamagnetic stored energy rises to only 1.7 τ_{EG}, the D-D reaction rate is only about half the value obtained in dipole phasing and finally the H-mode threshold value which is 5 to 7 MW in dipole needs to be 9 to 10 MW in monopole. A possible cause for the different behaviour is presented in the section "ICRH edge effects".

In Fig. 17, we summarize the global energy confinement obtained during H-modes with Beryllium screens. The energy stored in the fast particles $4(W_{dia} - W_{MHD})/3$ has been estimated. Typically, W_{fast} was 0.7 to 1.5 MJ or about 12 to 25 % of the total energy.

6.4. H-mode with Dipole Phasing and Gas Injection in the X-point Region. It is possible to delay the carbon bloom and to lengthen the duration of the H-mode by gas puffing in the X-point region. The gas puffing lasts during the entire duration of the experiment presented on Fig. 18. During the H-mode a secondary transition to a "Low Particle Confinement" Phase (LPC) takes place. The density starts decreasing at the LPC transition despite constant gas puffing. The radiated power and Z_{eff} also decrease during the LPC phase. The LPC allows the H-mode to last during the entire duration of the high power RF phase (2.8 s) at the expense of a 20 % reduction in energy confinement time but the particle confinement time was reduced by a much larger factor of about 3. The LPC phase corresponds to a higher level of the D_α emission with possibly " mini-elm" activity. This regime has a very similar performance to NBI H modes with gas puffing (Stork et al, 1991). However, this case does not show any of the giant elm activity present in the NBI case. This difference of behaviour may well be related to the short distance between the separatrix and the out-board limiters in the RF case. The LPC regime is a promising candidate for DC H-modes in a reactor where the particle and impurity confinement has to be kept low.

6.5. Deep Pellet Fuelling Combined with H-modes. Previous work (Jacquinot et al, 1988; Schmidt et al, 1989; Bhatnagar et al, 1989) has described the enhanced performance phase resulting from pellet injection penetrating up to the magnetic axis in non-sawtoothing plasmas ($q_o \simeq 1.2$ to 1.5). The subsequent re-heating phase exhibits a strongly increased D-D neutron production rate and improved central confinement. These modes were called PEP (Pellet Enhanced Phase). During the 1990 experimental campaign, it was possible to design discharges combining the confinement properties of the PEP to the H-mode (Tubbing et al, 1991; Kupschus et al, 1991). This new regime gives the highest thermo-nuclear yield.

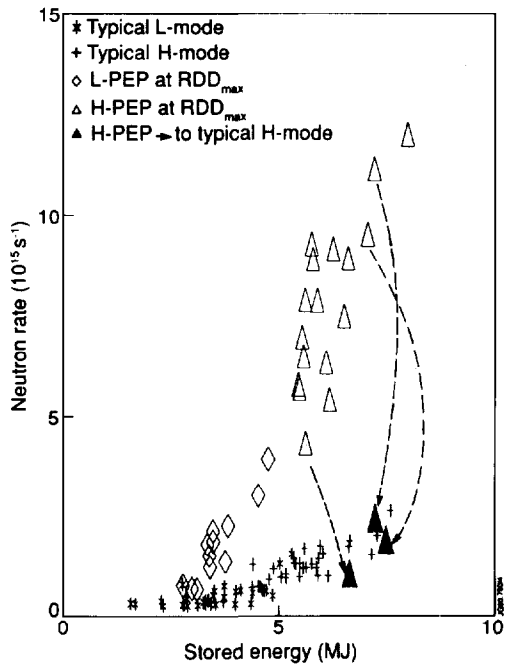

Fig 19: D-D neutron rate versus plasma energy for the various JET operating regimes.

Experiments are carried out in a double-null X-point configuration, with plasma currents between 3 and 3.6 MA and toroidal field between 2.8 and 3.2 T. A 4 mm pellet is injected at a velocity of 2.5 kms^{-1} at the beginning of the current plateau well before the onset of sawteeth. The pellet creates a peaked density profile with a central density of 1.5x10^{20} m^{-3}. The injection is followed (either immediately or with a delay of up to 1.5 s) by ICRH (Dipole phasing, 10 - 15 % H minority, resonance near the axis) and 2.5 MW of 80 kV neutral beam for diagnostic purposes. This leads, in less than 1 s, to equal central electron and ion temperatures of about 11 keV, a central density of about 7.10^{19} m^{-3} and a central electron pressure up to 1.2 bar at the time of the maximum D-D neutron rate of up to 10^{16} s^{-1}. 80 % of the neutron rate is of thermal origin. The maximum value of the fusion product $n_D(0).\tau_E.T_i(0)$ = 7.8 x 10^{20} m^{-3} s keV is obtained which is one of the highest seen on JET. After about 0.5 s, an L to H transition takes place and the total energy reaches up to 8 MJ. This PEP-H mode lasts about 0.5 s and reverts to an ordinary H-mode after a series of MHD events (Smeulders et al, 1991; Hugon et al, 1991). In Fig. 19, the peak neutron production rate of L- and H-mode plasma with and without PEP mode is plotted versus plasma energy demonstrating that the new PEP H-modes give typically 5 times more thermal yield than ordinary H-modes. They extend the previous PEP results by a factor 2. In Fig. 20, the normalised plasma energy content is plotted against the loss power. The figure shows that the global energy confinement of the best PEP H-modes is comparable or slightly better than that of ordinary H-modes.

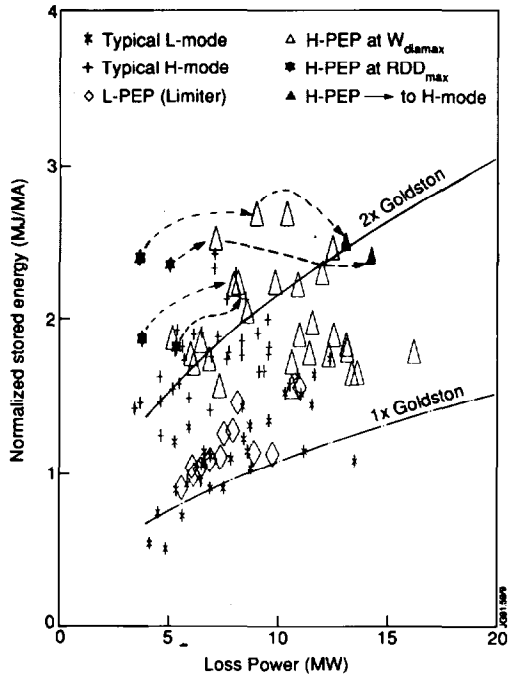

Fig 20: Normalized stored energy W_{dia}/I_P during various ICRF heated plasmas and, in particular, with deep pellet injection.

During the overlapping period of PEP and H-mode, local transport calculations using the FALCON and TRANSP codes have shown central values ($r \leq 0.4$ a) of the electron diffusion coefficient $D \approx 0.1$ m^2 s^{-1} and the effective heat conduction coefficient $\chi_{eff} \approx 0.5$ m^2 s^{-1}. Outside this region χ_{eff} values are found characteristic for H-modes with $\chi_{eff} \approx 1 - 2$ m^2 s^{-1}.

It should be stressed that the PEP H-mode experiment were conducted with a better ion heating efficiency from ICRH than previous experiments. This is due to operation at higher minority concentration, 10 - 15 % instead of 5 % with about 50 % ion heating (instead of 30 %). In some cases, this resulted in T_{io} being higher than T_{eo}. Figure 21 illustrates such a case and the highest ion temperature recorded with ICRH only $T_{io} \sim 14$ keV.

Detailed analysis suggests that the q profile is hollow during the PEP phase (Smeulders et al, 1991; Hugon et al, 1991). This conclusion comes from several concurrent indications: *(i)* MHD modes showing a 3/2 mode nested inside a 2/2 mode, *(ii)* calculation of the contribution of the bootstrap current, and *(iii)* position of the magnetic axis

for the observed pressure profiles. The initial onset of shear inversion may result from the hollow temperature profile created by the central pellet deposition. It is then maintained and amplified by the bootstrap current.

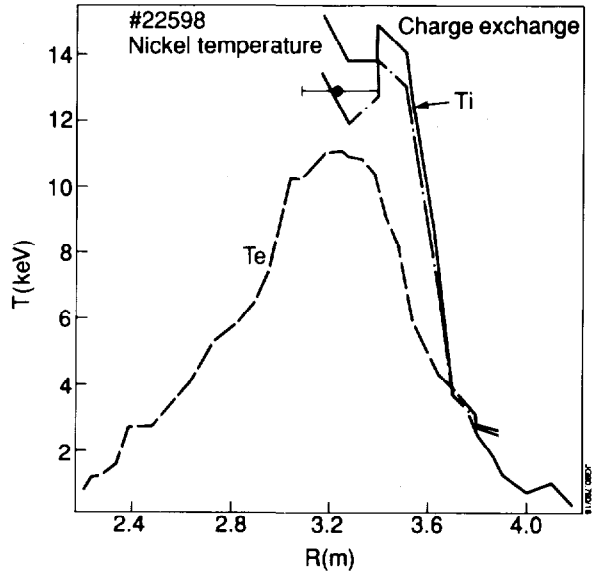

Fig 21: Ion and electron temperature profile during a PEP + H discharge at high H minority concentration giving $T_i > T_e$.

It is therefore possible that the enhanced confinement is associated with the reversal of the shear. Simulation using the Rebut-Lallia critical temperature gradient model outside the negative shear and neoclassical transport inside it shows qualitative agreement with the experiment before MHD activity sets in. Accepting this interpretation, one can propose that the mode could be sustained continuously with a precise radial profile of non-inductive current drive. This would imply driving most of the plasma current. A combination of TTMP (by ICRH) and EL (by LHCD) current drive would appear appropriate for this aim.

7. ICRH EDGE EFFECTS - CONVECTIVE CELLS

It has been known for some time that impurities are released from the screens of powered ICRF antennae. The flux depends on antenna voltage, plasma density near the screen, the angle of the screen bars to the magnetic field, the phasing and the material of the plasma facing components, in particular the screen bars (Bures, 1990). By replacing the nickel screens with beryllium, it was expected to reduce the impurity influx by virtue of the low sputtering coefficient of Be at the high energy (_ 0.2 to 0.6 kV) corresponding to the acceleration of the impurity ions (Be, O, C) in the sheath potential enhanced by RF field rectification.

Particularly significant are the sputtering coefficients of Be, C and O on Be which are well below unity even for the high RF sheath potential preventing the impurity avalanche process to occur (D'Ippolito et al, 1990). These favourable properties are also obtained from Boron or Carbon. Beryllium however is the best screen material since it has lower sputtering coefficients and offers, in addition, excellent electrical and mechanical properties which considerably ease the design of the screen. The release of the screen material during shows typical traces during such an experiment. The RF power is modulated in order to separate the emission from the screen (prompt signals) from the background which has a slow time response. With dipole phasing, the signals are much below any detectable levels (Fig. 22). With monopole phasing, the prompt modulated response of BeI and BeII increases with edge density and antenna voltage in agreement with the predictions of the RF sheath rectification model. The flux of Beryllium released by the screens depends on the other materials used in the immediate environment. Figure 23 shows that the Beryllium emission from nickel screens covered by a thin layer of Beryllium and used in combination with Carbon limiters give a larger Beryllium release than the same screens used with Beryllium limiters

suggesting that the sputtering of Carbon and Oxygen on the screen material can play an important role as expected in the theory.

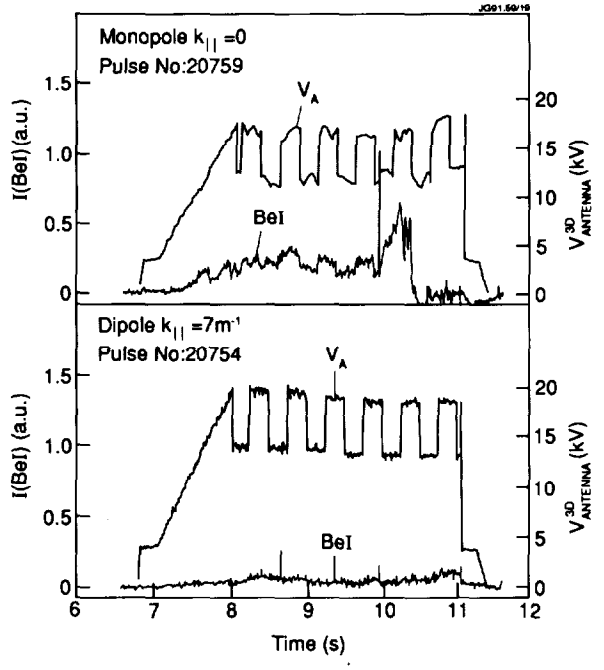

Fig 22: Intensity of the Beryllium line BeI emitted by the screens during modulated ICRH power. The prompt response identifies the specific ICRH impurity production.

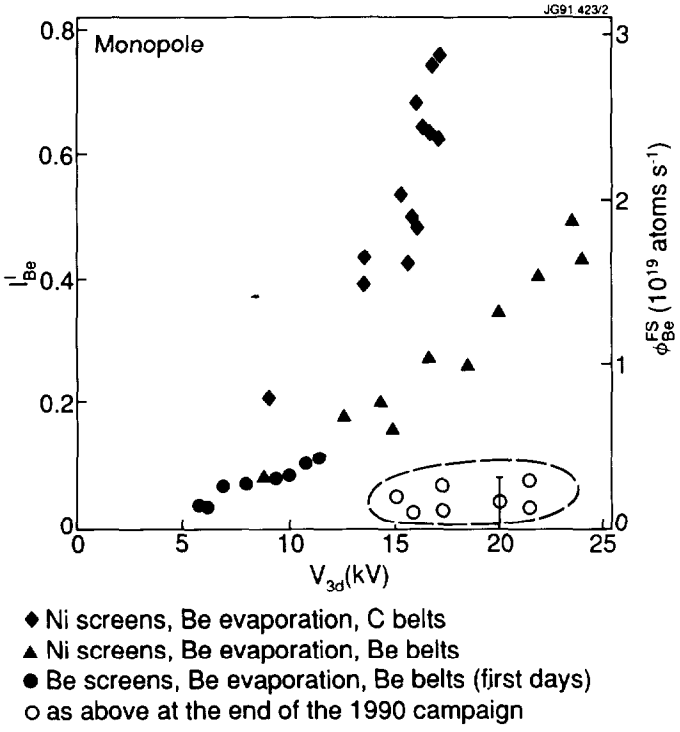

Fig 23: Intensity of the Beryllium line emitted by the ICRH screens and the corresponding beryllium influx Φ^{FS}_{Be} for various antenna, limiter and wall conditions.

In all cases, the absolute flux released by Beryllium screens is quite low. It can be expressed in terms of the related increase of Z_{eff}. We find that the specific ICRH impurity release corresponds to:

$$\Delta Z_{eff} = 0.005\ P_{RF}\ (MW)\ \text{for monopole, and}$$

$$\Delta Z_{eff} \simeq 0\ \text{for dipole}$$

Therefore specific ICRH impurity release can be entirely neglected in all conditions even at the highest power. This is also true with reverse toroidal magnetic field when the angle between the magnetic field and the screen bar is large (≈ 25°). However, in this case violent and intermittent arcing is observed on the screen with monopole phasing, presumably due to very high voltages appearing on the RF sheath. This arcing was never observed with dipole phasing.have been eliminated in all conditions. The RF sheath rectification model suggests that, edge effects should be fully eliminated only with dipole phasing or with the direction of the screen bars matching the direction of the magnetic field within ±1°. In fact, we have seen that H-modes with monopole phasing have a higher power threshold and give a lower energy confinement time. The steepening of the edge density profile during H-mode is also reduced (L de Kock et al, 1991). None of these effects, can be associated with a different impurity influx or a significant radiated power. We therefore conclude, that monopole phasing produces some modification of the plasma edge which is specific to ICRH.

The logical consequence of the RF sheath rectification theory is that this edge perturbation should take the form of a **convective cell**. The mechanism is sketched in Fig. 24. Each line of force linking 2 sides of the antenna is charged by the sheath rectification process to a DC potential. The potential is maximum for the line of force which crosses the largest RF flux; in JET, this line is nearly tangent to the antenna side protections. An electric field is therefore generated creating an ExB drift. As the electric potential returns to low values in the plasma, the drifts take the form of a convective cell. The convective cell has the size of the screen and is folded on itself over a thickness of some 4 cm. The penetration of the cell in the plasma is about 2 cm (D'Ippolito et al, 1991).

The theoretical analysis of the convective cell is still at an early stage but it is plausible that its perturbation of the edge is responsible for the inferior performance of the monopole H-mode. The convective cell is eliminated by the use of the dipole phasing. Its elimination in monopole phasing requires a precise alignment of the screen bars with the magnetic field.

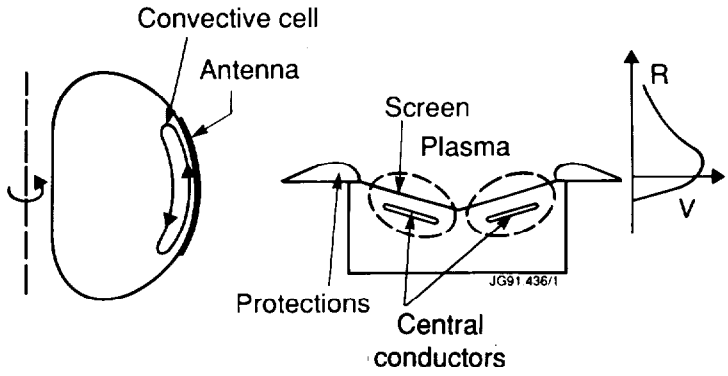

Fig 24: (a) Sketch of the potential charging the lines of force linking 2 sides of the antenna; (b) sketch of the resulting convective cell driven by E x B drifts.

8. CONCLUSIONS

In this article, we have summarized the results obtained during the 1990 experimental campaign of JET with the

2 RF systems. These 2 systems are in different stages of their development: the LHCD system has just started operation while the ICRH system is in a mature state having exceeded its initial design performance (22.3 MW coupled instead of 15 MW in the reference design) and having solved its specific impurity problem by proper antenna design.

The current drive results are quite encouraging: the localisation of the fast particles created by LHCD appears to follow expectations and the current drive efficiency is good even when some help given by TTMP is properly taken into account. This result confirms and extends the current drive efficiency reported by JT-60.

The first observation of the synergistic acceleration of the LHCD fast electrons by TTMP damping of the fast wave from the ICRH system is most interesting: in the short term, it provides JET with additional current drive capabilities for profile control (in particular to create shear reversal in steady state); in the long term, the synergistic LHCD and TTMP interaction or TTMP alone may well provide the ideal route for efficient current drive using electrons in the MeV range. This requires a parallel refractive index close to unity which can be generated using the fast wave monopole antenna.

Further current drive studies will include the increase of the LHCD power to 3 MW in 1991, 10 MW in 1993 and the development of an advanced launcher in 1994-95. The synergism of LHCD and ICRH will be increased by removing the main cyclotron resonance in the plasma enhancing the available TTMP power.

The new ICRH antenna design and in particular the choice of Beryllium as the screen material have fully met the expectations by removing the specific impurity generated by ICRH in all conditions. In addition, new feedback matching systems have allowed to maintain power coupling even during the large changes of the edge plasma during H-mode transitions. As a result of these upgrades, a new operating domain has been opened to studies using ICRH and taking advantage of its narrow and well-defined power deposition:

i) H-modes combined with "monster" sawteeth are routinely obtained with $\tau_E \geq 2.5\ \tau_{EG}$. A new mode with low particle confinement has been found.

ii) In L-modes, a ^{3}He-D fusion power of 140 kW has been generated in agreement with theoretical modelling. These experiments constitute a coherent benchmark of the (D)T scenario proposed for NET/ITER which minimizes the power required to reach ignition.

iii) The use of ICRH, led to the discovery of the PEP-H regime combining for the first time the good central confinement after deep pellet fuelling in the PEP mode to the confinement enhancement provided by the H mode.

A record thermal value of the triple fusion product $n_d\ \tau_E\ T_i$ of 7.8×10^{20} keV s m^{-3} was obtained in this way. Shear reversal was observed in this mode and, assuming that it is the cause for the enhanced confinement, continuous operation can be contemplated using current drive.

A new set of ICRH antenna is under construction. They will match the plasma geometry of JET in its pumped divertor configuration and provide a good directivity for TTMP current drive.

ACKNOWLEDGEMENTS

It is a pleasure to acknowledge the contributions of CEA (Cadarache) in the construction of one of the 2 prototype launchers and in component testing and of AEA (Culham) in theoretical modelling. We are also indebted to Drs M Cox, D Moreau, M O'Brien and G Tonon for valuable contributions in data analysis. Pellet injection results were obtained under a collaboration agreement between the JET Joint Undertaking and the US Department of Energy.

KEYWORDS

ICRH, LHCD, H-Mode, L-Mode, Heating, Confinement, Fusion Yield, Peaked Density Profiles, Antenna Screen, Edge Physics, Synergistic Effects, Current Drive

REFERENCES

Bhatnagar, V. P. et al (1989). Plasma Phys. and Controlled Fusion., **31**, 2111.
Bhatnagar, V. P. et al (1991). Plasma Phys. and Controlled Fusion., **33**, 99.
Bhatnagar, V. P. et al (1991). Contributed paper, these proceedings.
Bonoli P.and R. Englade (1986). Phys. Fluids **29**, 2937.
Brusati M. et al (1989). Proc 8th Top. Conf. on Radio Frequency Power in Plasmas, Irvine (Ca).
Bures M. et al (1990). JET-P(90)49; paper accepted for publication in Plasma Phys. and Controlled Fusion.
Chodura R. (1990). Fus. Eng. and Design, **12**, 111
Cordey J. et al (1991). Contributed paper, these proceedings.
Cottrell G. A. and D. F. H. Start (1991). Nucl. Fus., **31**, 61.
D'Ippolito D. et al (1991). Sherwood Fusion Theory Conf., Seattle, Washington and Lodestar report, L R C-90-18, and accepted for publication in Plasma Phys. and Controlled Fusion.
de Kock L. et al (1991). Contributed paper, these proceedings.
Eriksson L. (1991). Private communication.
Froissard P. et al (1991). Contributed paper, these proceedings.
Goldston et al (1984). Plasma Phys. and Controlled Fusion., **26**, 87.
Gormezano C. et al (1991). Contributed paper, these proceedings.
Hugon M. et al (1991). Submitted to Nucl. Fus.
Jacquinot J. and G. Sadler (1991). To be published in a special issue of Fus. Eng. and Design on D-^{3}He Fusion.
Jacquinot J. et al (1988). Plasma Phys. and Controlled Fus, **11**, 1467.
Jacquinot J. et al (1990). Fus. Eng. and Design **12**, 245.
Kovanen M. A. et al (1990). JET Joint Undertking, Abingdon (UK), Report JET-P(90)68
Kupschus P. (1991). Contributed paper, these proceedings.
Moreau D. et al (1989). Plasma Phys. and Controlled Fusion, **31** 1895.
Moreau D. et al (1991). Invited paper, these proceedings.
O'Brien M. and M. Cox (1991). Private communication.
Pain M. S. et al (1989). Proceeding of the 13th Symp. on Fus. Eng., Knoxville.
Perkins F. (1989). Nucl. Fus., **29**, 583.
Sadler G. et al (1991). Contributed paper, these proceedings.
Schmidt G. and the JET Team (1989). Plasma Phys. and Controlled Nucl. Fus. Research, Vol I, IAEA, Vienna, 215.
Smeulders, P. et al (1991). Contributed paper, these proceedings.
Start D. F. H. and the JET Team (1990). To appear in the proceedings of the IAEA, Washington, Conference.
Start D. F. H. et al (1990). JET-P(90)02, also published in Nucl. Fus.
Stix, T. H. (1975). Nucl. Fus., **15**, 737.
Stork D. et al (1991). Contributed paper, these proceedings.
Tubbing B. et al (1989). Nucl. Fus. **29**, 1953.
Tubbing B. et al (1991). Accepted for publication in Nucl. Fus.
Ushigusa K. et al (1990). Conf. proceeding of the 17th EPS Conference.

APPENDIX 1.

THE JET TEAM

JET Joint Undertaking, Abingdon, Oxon, OX14 3EA, U.K.

J.M.Adams[1], F.Alladio[4], H.Altmann, R.J.Anderson, G.Appruzzese, W.Bailey, B.Balet, D.V.Bartlett, L.R.Baylor[24], K.Behringer, A.C.Bell, P.Bertoldi, E.Bertolini, V.Bhatnagar, R.J.Bickerton, A.Boileau[3], T.Bonicelli, S.J.Booth, G.Bosia, M.Botman, D.Boyd[31], H.Brelen, H.Brinkschulte, M.Brusati, T.Budd, M.Bures, T.Businaro[4], H.Buttgereit, D.Cacaut, C.Caldwell-Nichols, D.J.Campbell, P.Card, J.Carwardine, G.Celentano, P.Chabert[27], C.D.Challis, A.Cheetham, J.Christiansen, C.Christodoulopoulos, P.Chuilon, R.Claesen, S.Clement[30], J.P.Coad, P.Colestock[6], S.Conroy[13], M.Cooke, S.Cooper, J.G.Cordey, W.Core, S.Corti, A.E.Costley, G.Cottrell, M.Cox[7], P.Cripwell[13], F.Crisanti[4], D.Cross, H.de Blank[16], J.de Haas[16], L.de Kock, E.Deksnis, G.B.Denne, G.Deschamps, G.Devillars, K.J.Dietz, J.Dobbing, S.E.Dorling, P.G.Doyle, D.F.Düchs, H.Duquenoy, A.Edwards, J.Ehrenberg[14], T.Elevant[12], W.Engelhardt, S.K.Erents[7], L.G.Eriksonn[5], M.Evrard[2], H.Falter, D.Flory, M.Forrest[7], C.Froger, K.Fullard, M.Gadeberg[11], A.Galetsas, R.Galvao[8], A.Gibson, R.D.Gill, A.Gondhalekar, C.Gordon, G.Gorini, C.Gormezano, N.A.Gottardi, C.Gowers, B.J.Green, F.S.Griph, M.Gryzinski[26], R.Haange, G.Hammett[6], W.Han[9], C.J.Hancock, P.J.Harbour, N.C.Hawkes[7], P.Haynes[7], T.Hellsten, J.L.Hemmerich, R.Hemsworth, R.F.Herzog, K.Hirsch[14], J.Hoekzema, W.A.Houlberg[24], J.How, M.Huart, A.Hubbard, T.P.Hughes[32], M.Hugon, M.Huguet, J.Jacquinot, O.N.Jarvis, T.C.Jernigan[24], E.Joffrin, E.M.Jones, L.P.D.F.Jones, T.T.C.Jones, J.Källne, A.Kaye, B.E.Keen, M.Keilhacker, G.J.Kelly, A.Khare[15], S.Knowlton, A.Konstantellos, M.Kovanen[21], P.Kupschus, P.Lallia, J.R.Last, L.Lauro-Taroni, M.Laux[33], K.Lawson[7], E.Lazzaro, M.Lennholm, X.Litaudon, P.Lomas, M.Lorentz-Gottardi[2], C.Lowry, G.Magyar, D.Maisonnier, M.Malacarne, V.Marchese, P.Massmann, L.McCarthy[28], G.McCracken[7], P.Mendonca, P.Meriguet, P.Micozzi[4], S.F.Mills, P.Millward, S.L.Milora[24], A.Moissonnier, P.L.Mondino, D.Moreau[17], P.Morgan, H.Morsi[14], G.Murphy, M.F.Nave, M.Newman, L.Nickesson, P.Nielsen, P.Noll, W.Obert, D.O'Brien, J.O'Rourke, M.G.Pacco-Düchs, M.Pain, S.Papastergiou, D.Pasini[20], M.Paume[27], N.Peacock[7], D.Pearson[13], F.Pegoraro, M.Pick, S.Pitcher[7], J.Plancoulaine, J-P.Poffé, F.Porcelli, R.Prentice, T.Raimondi, J.Ramette[17], J.M.Rax[27], C.Raymond, P-H.Rebut, J.Removille, F.Rimini, D.Robinson[7], A.Rolfe, R.T.Ross, L.Rossi, G.Rupprecht[14], R.Rushton, P.Rutter, H.C.Sack, G.Sadler, N.Salmon[13], H.Salzmann[14], A.Santagiustina, D.Schissel[25], P.H.Schild, M.Schmid, G.Schmidt[6], R.L.Shaw, A.Sibley, R.Simonini, J.Sips[16], P.Smeulders, J.Snipes, S.Sommers, L.Sonnerup, K.Sonnenberg, M.Stamp, P.Stangeby[19], D.Start, C.A.Steed, D.Stork, P.E.Stott, T.E.Stringer, D.Stubberfield, T.Sugie[18], D.Summers, H.Summers[20], J.Taboda-Duarte[22], J.Tagle[30], H.Tamnen, A.Tanga, A.Taroni, C.Tebaldi[23], A.Tesini, P.R.Thomas, E.Thompson, K.Thomsen[11], P.Trevalion, M.Tschudin, B.Tubbing, K.Uchino[29], E.Usselmann, H.van der Beken, M.von Hellermann, T.Wade, C.Walker, B.A.Wallander, M.Walravens, K.Walter, D.Ward, M.L.Watkins, J.Wesson, D.H.Wheeler, J.Wilks, U.Willen[12], D.Wilson, T.Winkel, C.Woodward, M.Wykes, I.D.Young, L.Zannelli, M.Zarnstorff[6], D.Zasche[14], J.W.Zwart.

PERMANENT ADDRESS

1. UKAEA, Harwell, Oxon. UK.
2. EUR-EB Association, LPP-ERM/KMS, B-1040 Brussels, Belgium.
3. Institute National des Récherches Scientifique, Quebec, Canada.
4. ENEA-CENTRO Di Frascati, I-00044 Frascati, Roma, Italy.
5. Chalmers University of Technology, Göteborg, Sweden.
6. Princeton Plasma Physics Laboratory, New Jersey, USA.
7. UKAEA Culham Laboratory, Abingdon, Oxon. UK.
8. Plasma Physics Laboratory, Space Research Institute, Sao José dos Campos, Brazil.
9. Institute of Mathematics, University of Oxford, UK.
10. CRPP/EPFL, 21 Avenue des Bains, CH-1007 Lausanne, Switzerland.
11. Risø National Laboratory, DK-4000 Roskilde, Denmark.
12. Swedish Energy Research Commission, S-10072 Stockholm, Sweden.
13. Imperial College of Science and Technology, University of London, UK.
14. Max Planck Institut für Plasmaphysik, D-8046 Garching bei München, FRG.
15. Institute for Plasma Research, Gandhinagar Bhat Gujat, India.
16. FOM Instituut voor Plasmafysica, 3430 Be Nieuwegein, The Netherlands.
17. Commissiariat à L'Energie Atomique, F-92260 Fontenay-aux-Roses, France.
18. JAERI, Tokai Research Establishment, Tokai-Mura, Naka-Gun, Japan.
19. Institute for Aerospace Studies, University of Toronto, Downsview, Ontario, Canada.
20. University of Strathclyde, Glasgow, G4 ONG, U.K.
21. Nuclear Engineering Laboratory, Lapeenranta University, Finland.
22. JNICT, Lisboa, Portugal.
23. Department of Mathematics, Univeristy of Bologna, Italy.
24. Oak Ridge National Laboratory, Oak Ridge, Tenn., USA.
25. G.A. Technologies, San Diego, California, USA.
26. Institute for Nuclear Studies, Swierk, Poland.
27. Commissiariat à l'Energie Atomique, Cadarache, France.
28. School of Physical Sciences, Flinders University of South Australia, South Australia SO42.
29. Kyushi University, Kasagu Fukuoka, Japan.
30. Centro de Investigaciones Energeticas Medioambientales y Techalogicas, Spain.
31. University of Maryland, College Park, Maryland, USA.
32. University of Essex, Colchester, UK.
33. Akademie de Wissenschaften, Berlin, DDR.

CR 88.49.1A